GEOLOGICA CARPATHICA, OCTOBER 2019, 70, 5, 373–385 doi: 10.2478/geoca-2019-0021

Deep gravity data interpretation using seismic reflection and well data: A case study of the West Gharib-Bakr area, Eastern Desert, Egypt

AHMAD A. AZAB

Egyptian Petroleum Research Institute (EPRI), Ahmad Alzomor Str. 2, Alzohoor District, Nasr City, Cairo, Egypt; research@epri.Sci.eg

(Manuscript received June 27, 2018; accepted in revised form June 13, 2019)

Abstract: A rigorous processing and analysis of the gravity data with seismic reflection and borehole information enabled a general view of the deep-seated regional structures in the West Gharib-Bakr area, Eastern Desert, Egypt. In this context, several interpretational techniques were applied to learn more about the supra-basement structures and intra-basement sources. The interpretation started with a review of the seismic data to clarify the structural elements on top of the Miocene strata, where a number of isochronous reflection maps were constructed and had migrated into depth maps. The Bouguer anomaly map was processed using Fast Fourier Transform filtering based on spectral analysis to separate the gravity anomalies into its components. Gravity stripping was also performed under the seismic isopachs and density controls. The gravity effect of each rock unit was calculated and progressively removed from the original data to obtain a new gravity map on top of the Pre-Miocene. To ensure more reliable results, further filtering and analytical processes were applied to the stripped map. The results of seismic analysis show simple structural configurations at the Miocene level, with a significant increase of evaporite thickness along the Gulf of Suez coast. In contrast, analysis of the stripped gravity map reveals a more intricate structure at the Pre-Miocene level, with increasing numbers/lengths of faults on the basement surface. Lineament analysis shows two major peaks trending N0–20°W and N50–70°E, produced by two main forces in NNW–SSE (compression) and ENE–WSW (tension) directions. The models confirmed a rough and ruptured basement surface, with no evidence of any magmatic intrusions penetrating the sediments. The basement relief map delineates five basins/sub-basins in the area which are separated from each other by ridges/saddles.

Keywords: West Bakr, Eastern Desert, Egypt, gravity stripping, applied geophysics.

Introduction

In deep basinal areas which contain excessive thickness of evaporite (Evp) rocks, such as the Gulf of Suez (GOS) area, the deep structural configurations are not clear enough. Seismically, the reflection data has several difficulties and large deficiencies at depths near the basement. The attenuation and dispersion of the energy of waves within the Evp group lead to the shortage of seismic data and bad events below the base of the Evps. In addition, most of the seismic surveys were acquired in the dip direction, which makes it difficult to delineate locations of the transform faults. Gravitationally, this may be attributed to the steepness of the GOS trend or to the great gravity effect of the near-surface layers. The structural/lithological variations of the Evps may create local anomalies like those arisomg from the Pre-Miocene (PM) features. All this may conceal the deeper sources and make it more difficult to determine locations of the uplifts and fault patterns. To overcome this, an integrated interpretation was carried out using all available geophysical data to disclose the hidden source structures on or within basement rocks.

The work started with interpreting the seismic sections through using the well logging information. The structural analysis focused on the shallow features capping the tops of the Miocene formations, where seismic lines seem to be very good in the upper part but very bad in the lower portion. The seismic interpretation is limited by the base of the evaporites, with most basic structural interpretation next to impossible. Therefore, the work has taken another way to interpret the deep configurations depending on the Bouguer gravity data. The interpretation is based on the fact that the gravity anomalies can be regarded as superposition of the anomalies reflected from the main density boundaries at varying depths. This means that the gravity anomaly includes effects of both shallow (residual) and deep (regional) constituents. Isolating either of them may enhance the effect of the other. In this context, two different enhancement procedures were applied to the Bouguer anomaly map with evaluation of their effectiveness in characterizing the deep-seated sources/structures. Firstly, the gravity filtering was performed using the Fast Fourier Transform technique to separate the gravity anomalies into residual and regional components. In fact, gravity filtering results were insufficient to give details about the deep configurations. Secondly, the layer stripping technique was applied as a more reliable interpretation method, where gravity, seismic and well data interpretation were integrated to disclose the hidden potential sources. To do this, the gravity effects of all shallow layers (Post-Miocene and Miocene rock units) were calculated and subtracted from the Bouguer data. The residue provides a stripped map on top of the PM that

conforms more with the deep constituents. This approach depends largely on the rock parameters, thickness and density of each formation. The formation-density has been derived from the drilled wells data, while the geometry of the formation was identified from the seismic isopach maps. Subsequently the stripped map on top of the PM was subjected to further analytical processes. The horizontal gradient filter and Euler deconvolution method were applied on top of the PM gravity map to map the main fault systems controlling the area. The lineaments analysis was performed to define the structural trends affecting the basic structure. A stress diagram and a strain ellipse were constructed to explain the different tectonic forces and associated shear fractures, which controlled the structural setup. The gravity modelling was done before and after gravity stripping to confirm the shallower structures, and to deduce the PM source structures. Finally, the source parameter imaging method was applied to determine the approximate depths of the basins and ridges, producing a map that more closely resembles the geology than originally.

The potential data used is the Bouguer anomaly map constructed from the ground surface. Askania torsion balance was used to construct a map with scale of 1:100,000 and contour interval of 0.5–1 mGal, in 1976. The gravity survey was carried out on the western coast of the GOS by Anglo Egyptian Oilfield Ltd., for the Egyptian General Petroleum Corporation (EGPC). The survey covers the area between Ras Bakr and Ras El-Bahar on the western coast of the gulf. The seismic data consists of fifteen seismic lines which was shot by Geosource Limited, on sept.,1981 under the auspice of the General Petroleum Company (GPC), for the (EGPC).

The aim of this work is to re-interpret all available geophysical data, in terms of structural setting and tectonic fabric, to shed light on deep source structures. The interpretation focuses on the PM uplifts and cross-faults that may be helpful in locating deep prospecting. Some emphasis was also placed on the distribution of basins and ridges in the area.

Structural considerations

The study area (Fig. 1) lies in the Eastern Desert along the western coast of the GOS, in the middle between Suez city to the north and Hurghada city to the south. It comprises several onshore oilfields, which are confined between the GOS to the east and Precambrian basement rocks of the Nubian to the west.

Grouping of blocks or sets of blocks having the same direction of dip lead to subdivision of the GOS into three tectonic provinces of contrasting dip attitudes, termed "Araba, Belayim, and Amal" from north to south. Each province is divided along major north-westerly trending faults into plates that almost plunge in the same direction (Mostafa 1976; Meshref 1990). The West Bakr oilfields lie in the central province of GOS, namely the north-easterly plunging Belayim province (Fig. 1) which is bounded from the north and south by two major faults or "hinge zones" of a NE–SW trend.

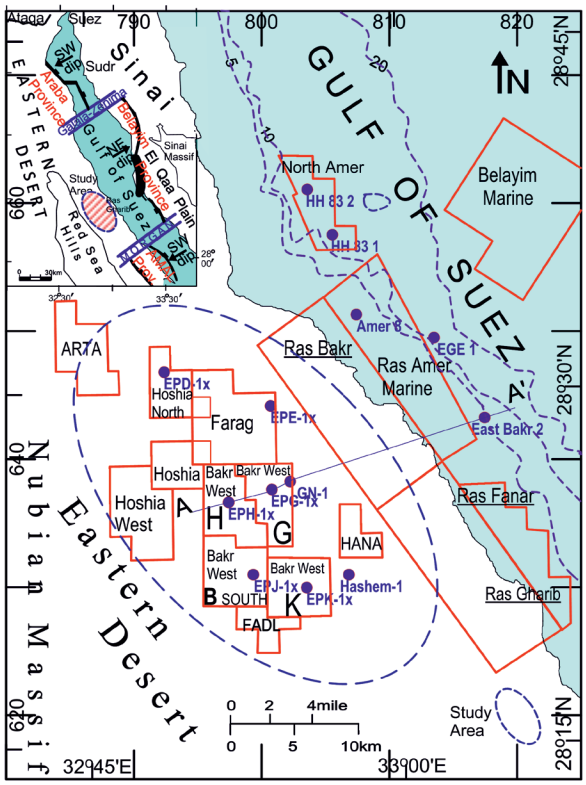

Fig. 1. Location map of West Gharib-Bakr area, with the oilfield concessions (see Appendix for GPS coordinates of the wells).

This province was separated from the Amal province by the "Morgan" hinge zone and from the Araba province by the "Galala-Zenima" hinge zone. The structure and sedimentology as well as the relationships between tectonics and sedimentation in the active Suez-rift basin were studied by many authors (e.g., Gupta et al. 1999; Young et al. 2002; Herkat & Guiraud 2006; Khalil & McClay 2008; Pietrantonio 2016; Rohais et al. 2016; Bosworth & Durocher 2017; Segev 2017; Azab 2018).

The drillhole information in the study area indicates a thick sedimentary section of the PM and younger rocks, unconformably overlying the basement complex (Ghanim 1972; Scotte & Govean 1984). The sedimentary section comprises rocks of Carboniferous, Cretaceous, Paleocene, Eocene, Miocene and Pliocene-recent ages (Shabaan et al. 1984). The Miocene rocks are the main source of oil-bearing rocks and they vary from place to place. They are divided into lower clastic rocks (Gharandal group) and upper evaporitic rocks (Ras Malsab group). The Gharandal group includes the (Nukhul, Rudeis and Kareem fms.) that underlie the Evps of the Ras Malaab group (Belayim, South Gharib and Zeit fms.). The Evp rocks consist mainly of anhydrite, gypsum, salt rocks intercalated with shale and sandstone. The PM sediments are generally characterized by a wide distribution and great thickness of the clastic rocks. The crystalline basement rocks seem to be quite similar to those cropping out to the west of the area (Mostafa 1992).

Previous works in the study area (Otsuka & Ogawa 1977; Shabaan 1984) indicate that the west Gharib-Bakr area is

characterized by thick layers of Evps that exist in Kareem to Zeit fms. and act as sealing rocks. The Evp group shows large lithological variations, and consists of anhydrite (high density) and salt-halite (low density), contaminated with shale, sands, lime (medium density). The percentage of these rocks vary laterally/vertically and lead to significant changes in the bulk density from one place to another. Generally, the density of the Miocene Evps varies widely from 1.9 to 2.9 g/cm^3, based on the percentage of anhydrite compared to other sediments.

Seismic interpretation

The structural configuration in the study area was studied through interpreting fifteen 2D seismic lines vibrated in the NW and NE directions. These seismic sections were carefully inspected to detect the most reliable marker horizons. The available well velocity survey of Hashem-1 (Miocene/TD 2909 m), EPH-1X (Cenomanian/TD 2659.98 m) and EPG-1X (Nubia/TD 2915 m), and their composite well logs were used to facilitate the identification of the real reflectors in the seismic records. The strong/continuous reflectors on the tops of the Evp layers were easily traced along the seismic lines. The subsurface geological identification was done through picking and correlation of reflection times as well as fault detection. Analysis of the seismic sections was limited by the base Kareem Fm., which is the deepest horizon of seismic interpretation. Accordingly, several isochronous reflection maps were established through picking the two-way times (Fig. 2). The average velocity and isochronous reflection maps on top of the different formations were used to convert the reflection times into depths. The structure contour maps in terms of depth and faulting were also constructed on the tops of the Miocene formations (Fig. 3). Close correlation between these maps shows that the Miocene rocks are affected by a small number of faults that increase in number and length with depth. The faults run mainly in the NW–SE direction (GOS trend) while the NE–SW cross-gulf faults are absent. In addition, the isopach maps for post-Zeit, Zeit, South Gharib, Belayim and Kareem were constructed from the grid-data of the depth contour maps, whilst the isopach map for the Lower-Miocene Rudeis Fm. is constructed based on the composite logs of the drilled wells. The isopach maps indicate presence of a large thickness of Evp sediments in the north-east part, while Lower-Miocene Rudeis sands increase in a south-west direction.

Seismic profiling was established to show the lateral/vertical subsurface distributions more clearly. A geoseismic section BK-1039 (Fig. 4) is displayed as an example in the NE–SW dip direction, constructed through transforming the seismic reflection time into depth using the well velocity data. Generally, the seismic line seems to be very good at shallow depths where it shows strong reflections corresponding to the high density/velocity Evps. Noticeably, the post-Evps/Evps decrease in their thickness towards the south-west, and significantly increase toward the north-east before diminishing over the offshore ridge (Bakr-Gharib), a fact that was

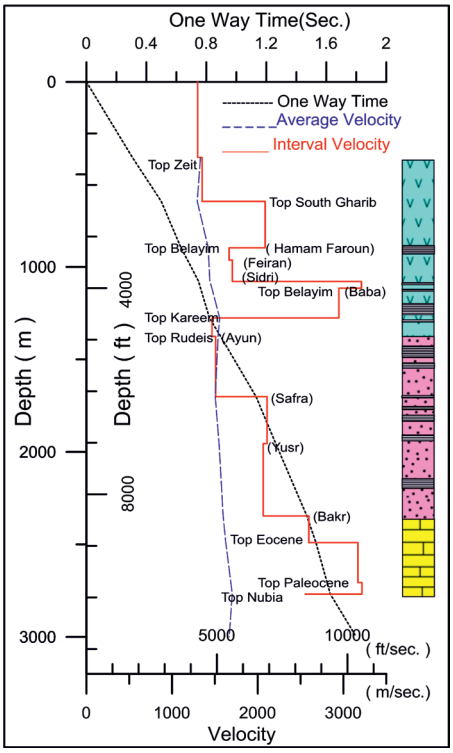

Fig. 2. Time-depth curve and velocity analysis of Hashem-1 Well.

verified by well data. The seismic line shows that a small number of short fractures cut across the Miocene strata. These normal faults have small throws and do not reach the surface where the surface layer seems to be not entirely deformed. As expected, seismic evidence is generally very poor at large depths, where the continuity of the seismic events is markedly bad beneath the Kareem Fm. There is no evidence to support the presence of faults below the Miocene Evps. If they are present, it is rather difficult to judge whether such bad events relate to deep fault-structures or are due to lithological variations. Generally, seismic interpretation had failed to give any exact information about locations, orientations, magnitudes or throws of faults below the Evp rocks. Seismic reflection is also ineffective for locating the PM high-structures, caused by basement uplifts.

The seismic interpretation was confirmed by a SW–NE geological cross section AA' (Fig. 5), which extends between four wells drilled in the study area. The cross section shows a structural uplift at the EPH-1, EPG-1 and GN-1 wells, where the thickness of the formations is reduced and the formation tops have less depth. Eastward, the structure exhibits a real increase in thickness of the sedimentary section alongside the GOS coast, especially of the Miocene and Post-Miocene sediments. This Miocene basin is bounded from the east by an uplifted block (Bakr-ridge), where PM rocks are shallower at Bakr-2. Westward, the basement rocks were buried under thick sections of the PM and Lower-Miocene sediments. The Miocene layers were affected by a number of normal faults that extend downward and are thought to be inherited from older tectonics.

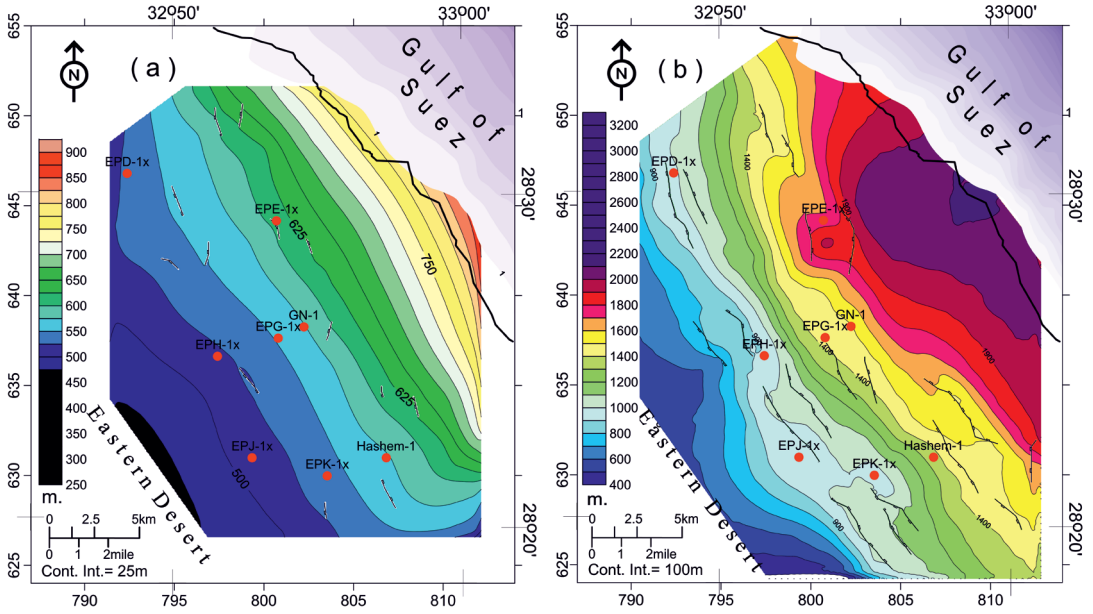

Fig. 3. Structure-depth contour map: **a** — on top of Zeit Formation/top Miocene section; **b** — on top of Rudeis Formation/base of Miocene-evaporites.

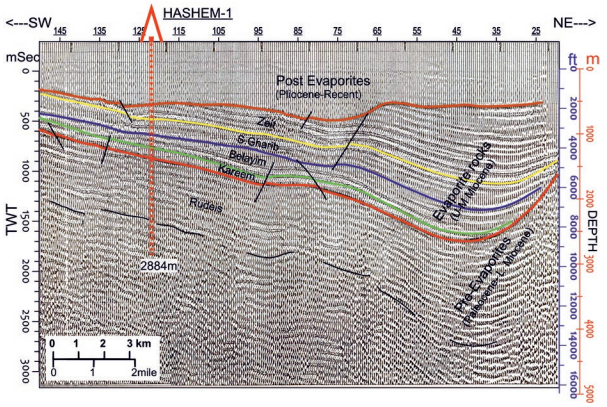

Fig. 4. Interpreted geoseismic line BK-1039 along NE–SW direction.

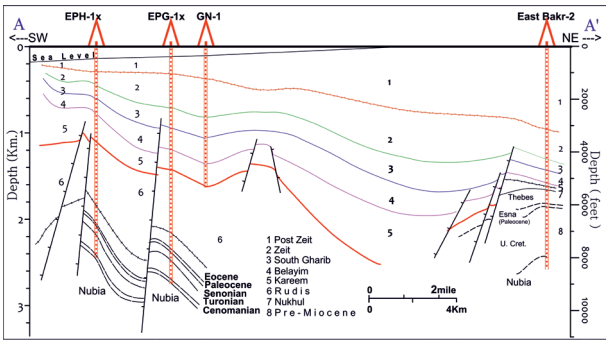

Fig. 5. Geological cross section A–A', taken in the NE–SW direction, passing through EPH-1X, EPG-1X, GN-1 and E. Bakr-2 wells.

Gravity interpretation

The Bouguer anomaly map (Fig. 6) shows dominance of the negative gravity values from −35 to −51 mGal all over the area, which may reflect a relatively thick sedimentary cover. The gravity field is largely variable from east to west, which may be associated with large lithological/structural variations in the subsurface. Qualitatively, the map contains a number of strong anomalous features of different amplitudes and sizes, running nearly parallel to the GOS trend. The high and low gravity zones are separated from each other by steep gradients, which strike in the north-west direction. Such high gravity gradient zones were traced on the Bouguer anomaly map by circles of Euler solutions, which tend to cluster along geological boundaries. The linear structures are closely associated with locations of major bounding faults, which divided the area into a number of gravity zones of a north-west orientation. Little or no solutions tend to cluster along the transform-fault traces. Generally, the gravity maxima and gravity minima are closely linked with the major structural features in the area. For instance, the high gravity anomaly that exists along the offshore part corresponds to the pre-existing horst blocks extending from Amer to Gharib. The West Bakr oilfields (G, H, B and K) could also be correlated with high anomalous features. Westward, the gravity low corresponds to a broad sedimentary basin of "Khashaba low", while the gravity maximum in the south-western corner is related to basement outcrop of the Nubian Massif.

To separate the gravity anomalies into their components, the Fast Fourier Transform matched filtering technique based on spectral analysis was applied to the Bouguer anomaly map. The isolation method depends mainly on the slopes of the spectral analysis curve, where the frequency ranges give the most efficient estimation of the gravity anomalies to fit the deep and shallow constituents. The separation using the energy spectrum of potential field data is highly advantageous over any other known conventional method (Sadek 1984). The potential anomalies in the space domain are transformed into

frequency domain and the various parameters of anomaly sources are derived from the characteristic properties of the amplitude. Moreover, the spectral method provides the possibility of doing depth measurement using gradients when no anomalies are expressed in the profile. The theoretical assumption was studied by many authors. Spector & Battacharyya (1966) computed the energy spectrum and autocorrelation function of FFT for the simple magnetic model. Spector (1968) shows that the energy spectrum is greatly affected by surface highs above the basement, the greater the high the longer the wavelengths. The anomalies and autocorrelation functions associated with simple 2-D (two-dimensional) and 3-D (three dimensional) magnetic and gravity models were subsequently transformed mathematically to the frequency domain by Spector & Bhattacharyya (1966). Spector & Grant (1970) reported some undesired effects on the calculations of the energy spectrum which derive from processes of digitization, quality and density of data. Dimri (1992) and Blakely (1995) estimated the mean depth of the interfaces considering the log of power of the Bouguer gravity spectrum as a function of wavenumber/frequency assuming uncorrelated distribution of sources (Spector & Grant 1970) or scaling nature of sources (Pilkington et al. 1994; Maus & Dimri 1994, 1995, 1996).

Isolation of the gravity anomalies was carried out using Geosoft 2007 software and the results are shown in Figure 7a. Two linear segments of the energy decay curve with distinguishable slopes were used to isolate the regional and residual components, where the regional effects are evident at larger wavelengths and the shallow/local effects are evident in short wavelengths. Accordingly, the energy spectrum curve involves two parts: a very steep part at low wavenumbers (0 km^{-1}-<wavenumber<0.230 km^{-1}) and a less steep part at high wavenumbers (0.230 km^{-1} < wavenumber < 1.400 km^{-1}). The depth can be estimated by $h = -s/4\pi$ where: (h) is depth; (s) is slope of log (energy) spectrum. Accordingly, the slope of the line fitted to the upper part of the spectrum curve is used to estimate the average depth of deep sources (~24 km), and the average depth to shallow sources (~4.5 km). The frequency bands related to the regional and residual gravity components on the energy spectrum were used through the band-pass filtering. By bandpass, all wavenumbers between limited values would be saved or passed while the rest would be cut, so that the bandpass filter passes frequencies within a certain range while rejecting frequencies outside this range.

The high-pass gravity map (Fig. 7b) shows a set of sharp anomalous zones which are closely correlated with the shallow components. The residual gravity field reveals improvements of the gravity anomalies linked with near-surface constituents, but still lack details about deep-seated constituents. Thus, it is

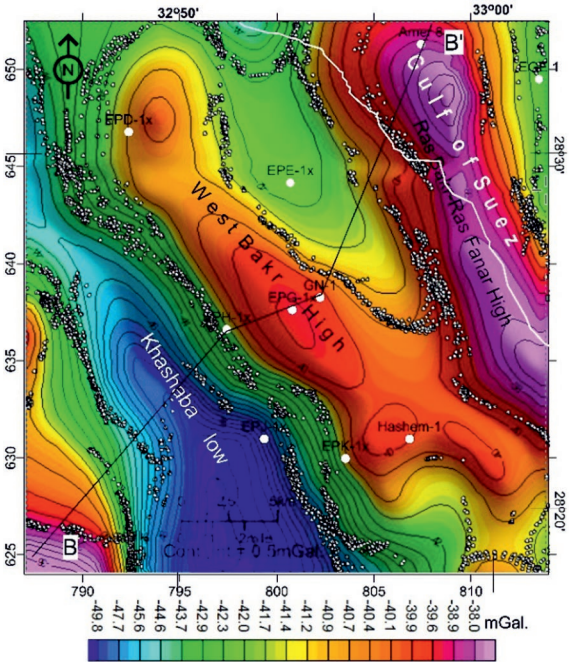

Fig. 6. Bouguer anomaly map of the study area overlapped with the Euler deconvolution solutions (SI=0, window size=10).

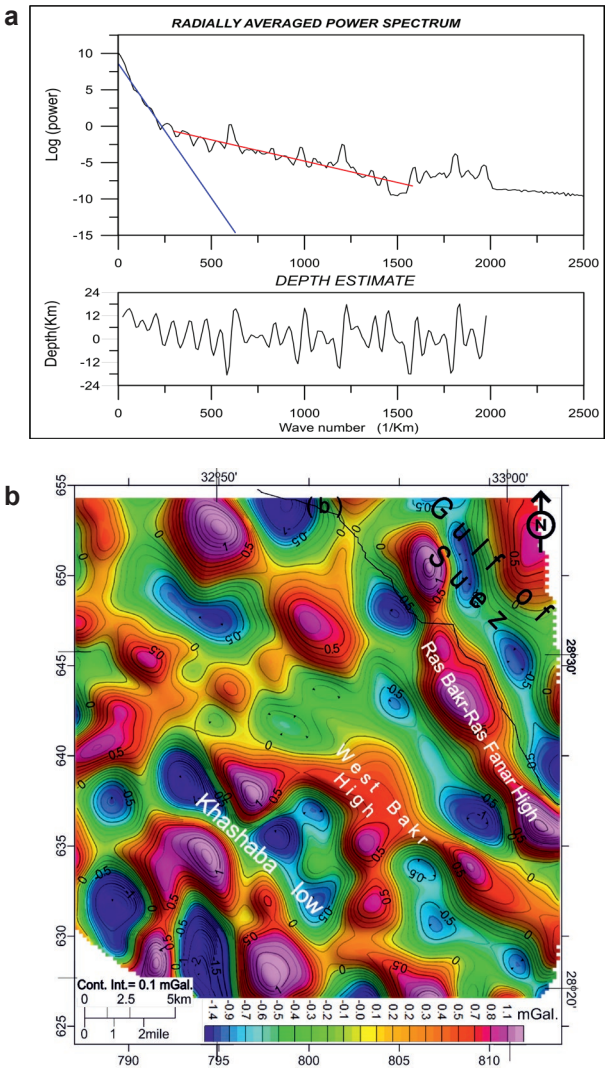

Fig. 7. a — Power spectrum of the Bouguer anomaly map, with two linear segments of the energy decay curve with distinguishable slopes. **b** — High-Pass filtered map of the Bouguer gravity data at the high frequency and short wavelength range (230 cycle/km<wavenumber <1400 cycle/km).

found that the filtered map does not meet the requirements for studying the deep source structures.

Combined gravity–seismic interpretation

In fact, both seismic and gravity interpretations are unable to reflect the deep causative source bodies due to strong shielding of the evaporitic rocks. The large thickness of Miocene Evps inhibits even the strong seismic energy to refract into the deeper horizons. Likewise, gravity anomalies are very sensitive to the thickness/density variations of the anhydrite-salt rocks. Consequently, it is deemed necessary to use an integration of the gravity and seismic in combination with well information to interpret deep source structures. This was done through applying the gravity stripping technique based on Hammer (1963) and Otsuka & Ogawa (1977). The gravity stripping depends on computing the gravity effect of a certain rock unit or time-rock unit defined by its thickness and density, then subtracting the effect from the integrated effect of the whole sedimentary section, as has been indicated by the Bouguer anomaly map, to get the pre-unit effect, and so on for the other units (Parker 1973). This requires an exact knowledge of the rock properties (geometry and density) to get good results.

The workable equation applied for each rock unit in the sedimentary succession is

$$\Delta g_i = 2\pi\, G\, \Delta\rho\, H_i \qquad (1)$$

where Δg_i is the gravity effect of a certain rock unit in mGal; G is the international gravitational constant (6.67×10^{-8} cm^3/g.s^2); $\Delta\rho$ is the density contrast between the formation density and the basement density in g/cm^3; H_i is the unit thickness in cm.

The depths to the upper and lower surfaces of each rock unit have been seismically controlled. The thicknesses of the layers were calculated through a number of seismic isopachs (thickness-grids). The formation density was taken from the density logs (gamma–gamma) for about eleven drilled wells, which were checked and used to construct a set of density gradient maps (Fig. 8). For every drilled well, the density log measurements against each formation in the succession were averaged and used as a single value for that formation. Figure 9 is an example for density information derived from the Bakr-2 and Hashem-1 wells. They represent two different time intervals, Bakr-2 Well displays densities of the PM section while Hashem-1Well shows the densities of the Miocene section.

From the obtained thickness-grid and density-grid of each rock unit, the gravity effect for every layer was calculated and subtracted/removed from the observed data. The process was repeated for all formations in the sequence from the surface to the datum. In each case, two maps were obtained; the first map represents the sum of gravity effects of all formations above the datum. The second represents the gravity effect of the rock units below the datum. At last, a stripped gravity map on top of PM was obtained which could be correlated with the original.

Generally, the gravity effects of the Evp group are given by

$$\Delta g_{evp} = 2\pi\, G\, ((\rho_{zeit}-\rho_{Bas})h_{zeit} + (\rho_{SG}-\rho_{Bas})h_{SG} + \\ + (\rho_{Bel}-\rho_{Bas})h_{Bel} + (\rho_{kar}-\rho_{Bas})h_{kar}). \qquad (2)$$

The stripped gravity map on top of PM sequence can be given by the relation

$$\Delta g_{strip} = \Delta g_{Boug} - (\Delta g_{PM} + \Delta g_{MM} + \Delta g_{LM}). \qquad (3)$$

The above relations were applied using Surfer 13 Golden Software where the outputs were calculated and contoured.

Figure 10a shows the sum of gravity effects due to sedimentary section above the datum (surface layer, Miocene Evps and Lower-Miocene clastics). The map is generally characterized by a negative gravity effect (from −1 to −7 mGal), that increases progressively from north-east to south-west. Figure 10b presents the stripped gravity map on top of the PM after removing the effects of the overlying formations from the original data. The map shows the largest gravity effects with negative values (from −20 to −49 mGal), which gradually increase toward the south-east. This may reveal that the gravity effect of the PM is the main source of negative gravity present in the Bouguer map.

The correlation coefficient that measures and determines the degree to which two variables are associated, was calculated between the gravity data before and after the stripping process. The results in Table 1 shows a positive correlation between the data of Bouguer and data for gravity effects on top of the PM. Meanwhile it gives negative correlation versus others, particularly against the Evp group (Fig. 11). The positive value may suggest that the deep causative sources have the highest gravity effect, while the negative value may reflect a gravity effect in the opposite direction. Accordingly, it could be stated that, despite the large gravity effect of shallower structures, the deeper sources are still the most effective.

The horizontal gradient method (Phillips 1998) was applied on the stripped map (Fig. 10b) with the goal of revealing the hidden faults. The horizontal gradient maxima delineate the approximate locations, lengths and trends of the major faults on/within the basement rocks. Figure 12a displays two main trend patterns, cut cross the study area in the NNW (Clysmic) and ENE (Syrian arc). Generally, the structure on top of PM in Figure 12a shows dense fractures/faults if compared with the Miocene structure in Figure 3. These lineaments were traced and statistically analysed (Affleck 1963) in terms of number, length and direction to reveal the basic tectonic trends. Figure 12b shows two major peaks in the N0–30°W and N50–70°E directions. These two major peaks demarcate two main fault systems (cross-faults) which are predominant on the basement surface and divided the area into segments. The structure suggests presence of a NE–SW trending shear fault zone, with a left-lateral displacement, in the centre of the map.

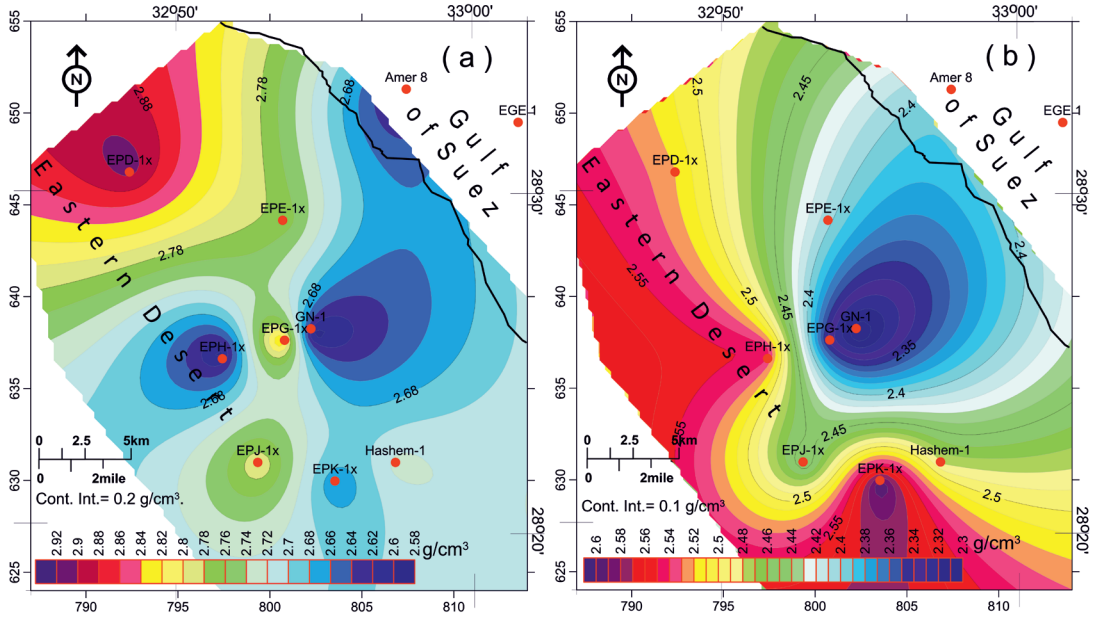

Fig. 8. Formation density gradient map of the (**a**) Post-Miocene and Miocene evaporites, and (**b**) Lower-Miocene Rudeis sands.

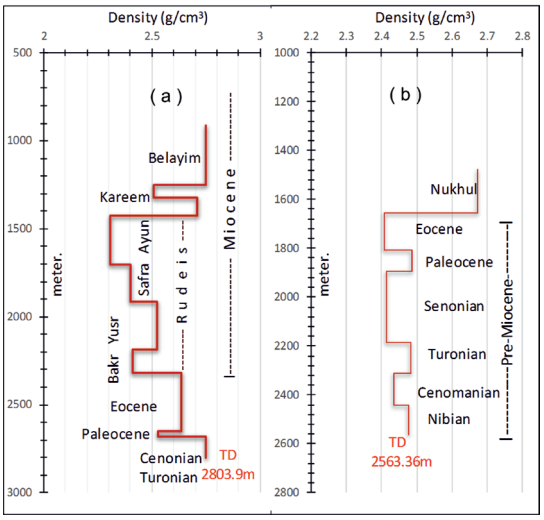

Fig. 9. Density log of (**a**) Hashem-1 Well, and (**b**) Bakr-2 Well.

Stress fields and proposed tectonic model

According to the trend analysis results shown in Figure 12b an attempt was made to deduce the stresses and their possible relations with the crustal deformation and plate motion which affect the area (in-house software). Detected trends interpreted from the gravity map after stripping were used in combination with the idea of possible reorientation of stress (McKinstry 1953) to shed light on the direction and intensity of stresses explaining the tectonism of the area. Figure 12c shows that Precambrian basement is controlled by two different forces acting on the region for long periods of time. The area was subjected to a regional compressive stress in NNW direction, contemporaneous with ENE extension force. The first compressive stress is oriented N10°W. It is believed to be associated with the collision between the African and European plates. This principal axis of stress seems to have shifted toward the west during different geological times, with a wide azimuth of N0–30°W. Structurally, this stress force resulted in two sets of primary and secondary shear fractures. The main structural lines produced by the first stress force were formed as primary shear fractures in a NNW–SSE direction. The ENE folding/thrust faulting was also formed perpendicular to the greatest principal axis of this type of stress force. Besides, the N35°W (Clysmic) and N15°E (Aqaba) arose as secondary strike-slip faults, where the angle between these two sets of the sinistral and dextral fault systems is about 50° (Anderson 1951). The second force affected the area is the tensional N85°E, which is attributed to the movement of the Arabian plate relative to the Nubian Plate. The structural elements produced by this tectonic extension primarily take the form of the N5°W Clysmic fault system. The N50–70°E trend is considered as a second order fault system produced by these extensional forces. The rejuvenation of these tectonic trends during different episodes may explain the high peak of N50–70°E. The principal axis of this tensional force seems to have rotated counter-clockwise. A reasonable model explaining the tectonism in the GOS-Red Sea region was proposed by Bayoumi (1983), to sketch the expected structural/tectonic development during its geological history.

Deep structural elements

The Euler homogeneity relationship was used as an automated method to derive the plan location and depth estimation of buried objects from the gridded-data. Euler's homogeneity equation relates the gravity field and its gradient components

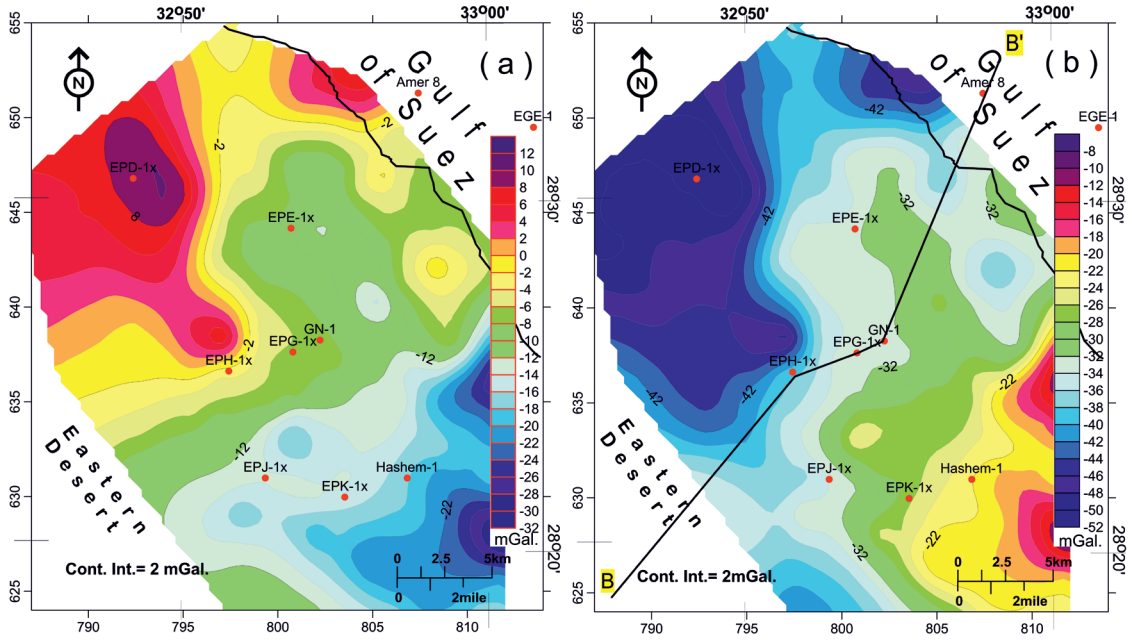

Fig. 10. Gravity effect of the sedimentary section: **a** — above the datum due to the Post-Miocene surface layer, Miocene evaporites and Lower Miocene Rudeis sands; **b** — below the datum on top of Pre-Miocene.

Table 1: Correlation coefficient results of different gravity effects

Correl Coef between	Results
Boug /Pre-Miocene	0.34582
Boug /Rudeis	−0.10386
Boug /Evaporite	−0.33758
Boug /Post-Zeit	−0.03948

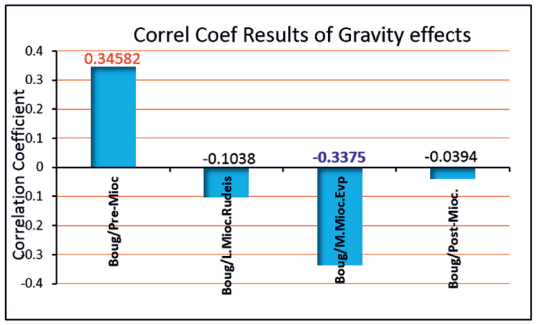

Fig. 11. Correlation coefficient between the gravity data before and after stripping process.

to the location of the source with the degree of homogeneity expressed as a structural index (SI; Thompson 1982). The structural index is a measure of the rate of change with distance of the field from the source (fall-off rate) and is directly related to the source dimension. Depth and structural index "solutions" provide information about the source of anomalies. The advantage of the Euler Deconvolution (ED) technique over other depth interpretation methods is that no particular geological model is assumed, and can be directly applied to large gridded data sets. The process reduces significantly the time required for analysis of the data, it requires no prior knowledge of the source of gravitation/magnetization direction and assumes no particular interpretation model (Barbosa et al. 1999; Hinze et al. 2013). The method can locate or outline the confined sources, dykes and contacts with remarkable accuracy (Reid et al. 1990). Marson & Klingele (1993) applied it to gravity vertical gradients. Zhang et al. (2000) applied it to gravity tensor gradient data. The Euler deconvolution is used to confirm the modelling results, because it is both a boundary finder and a depth estimator (Reid et al. 2003).

The ED was applied to the stripped gravity map (Fig. 10b) to deduce the major structural elements on top of the PM/basement rocks. Herein, the structural insides of SI=0 were used to identify the rock boundaries and to estimate the depths of their sources (Thompson 1982 and Reid et al.1990). The calculation is running for window size (10) to obtain solutions for different depths.

Figure 13 provides the best solution for the block-faults with depths ranging from 0 to 4 km on top of the PM (without depth of the overlying). The interpretation is based on the linear solutions that mark the geological boundaries and divided the area into blocks. These linear features tend to occupy zones of high gradients between anomalies. The distributions and depths were identified using coloured circles, overlapped on a shaded relief map. The white circles indicate shallow depths while red circles locate deep faults. Generally, the map reflects the complex structure on the basement surface through a set of major faults that are bordering the main structural features in the area. Most of these linear representations (major faults) westerly-oriented in the NNW direction, parallel to the axis of the GOS. The Clysmic trend is not a long-continuous feature, but was dissected and displaced by faults oriented in

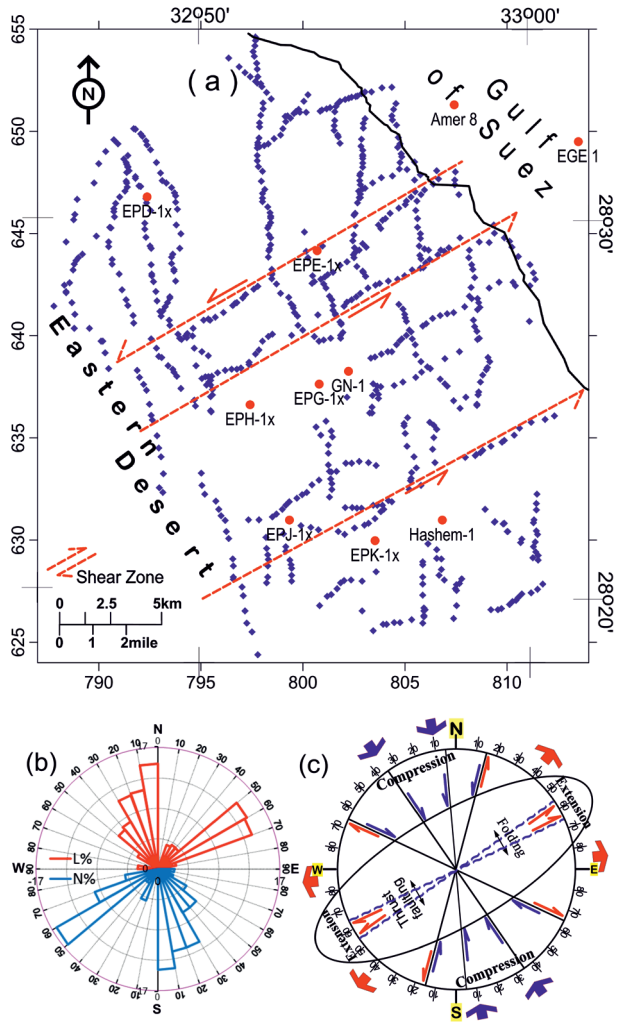

Fig. 12. a — Maxima of horizontal gradient magnitude of the stripped gravity map on top of Pre-Miocene. **b** — Rose diagram of tectonic trends as deduced from the stripped map on top of Pre-Miocene. **c** — stress-strain diagram of the study area based on statistical trend analysis.

an ENE direction. Some circles may be poorly-clustered, where there is no significant density contrast, while, the large condensation of circles may be due to dipping faults at large depths, or upward reactivation of these trends. Generally, the fault trends interpreted from ED in Figure 13 agree with those shown in Figure 12. In comparison with seismic results, the structure on top of the PM (Fig. 13) is more complicated than that at the Miocene level (Fig. 3).

Gravity modelling

The profile B–B' was taken on the Bouguer anomaly map (Fig. 6) and on the stripped map (Fig. 10b) cutting across the central part in a SW–NE direction. The profile stretches for about 35 km, passing through four drilled wells (EPH-1X, EPG-1X, GN-1X, AMER-8) which are considered as controls and start points. The sedimentary layers were modelled as 2D

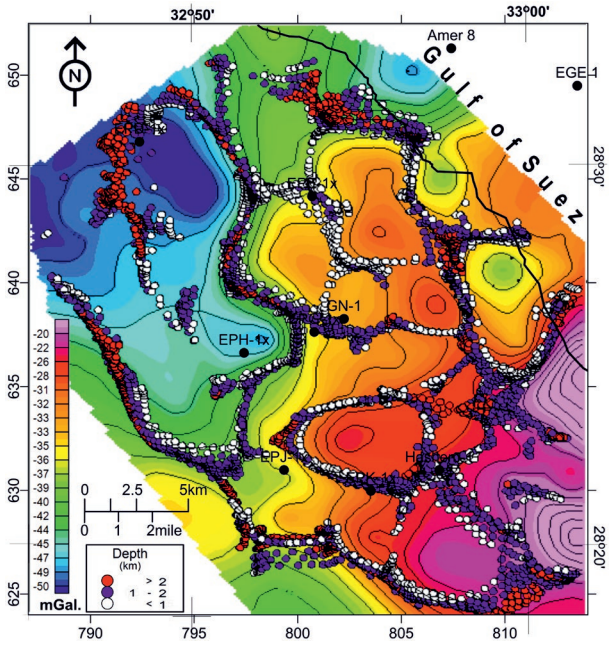

Fig. 13. Euler deconvolution results on top of Pre-Miocene as deduced from the stripped map.

units, where X-axis (strike-length) is long relative to Y-axis (depth). The sedimentary sequence consists of three main groups with different lithological characteristics; the post-Evps (~2200 kg/m^3); Evps (~2800 kg/m^3); pre-Evps (~2540 kg/m^3). The rock parameters were constrained by the seismic isopachs (geometry) and by information derived from boreholes (density). The basement density was found to be 2670 kg/m^3, where there is no magmatic intrusion in the area (Shabaan et al. 1984). The modelling process was done using GM-sys, included in the Oasis Montage Package (2007).

Figure 14a presents a model for the regional subsurface structure (shallow and deep) before doing the stripping process. The upper part shows a good fit between the calculated and observed gravity profiles. The lower part exhibits great changes in the depth to the basement from the west to east, with a regional dip regime to the west. The basement surface is uneven/rough and loaded by thick and thin sedimentary sections that conceal beneath it more complicated structures. Generally, topography of the basement is in harmony with gravity anomalies where the swells and troughs are correlated with gravity maxima and minima, respectively. The model exhibits two deep basinal areas in both sides, these are; the PM basin to the west (Khashaba low) in parallel to the Nubian Massif, and Miocene basin to the east (W. Bakr basin) alongside the GOS. These two basins are correlated with low gravity anomalies, and are separated from each other by a ridge-like form (W. Bakr high). The structure exhibits a number of major faults separating the main topographic features. These normal faults arise on the basement surface, grow upwards into the PM section and mostly disappear into Miocene formations.

Figure 14b presents a sketch of the modelled profile after doing the gravity stripping. Here, the gravity effect due to the upper part of sedimentary cover was neglected since densities

of the Miocene and Post-Miocene were found to be zero. The removal of the gravity effect of the shallower portion gives a chance to better model the deeper structures. The deep source structures were deduced through matching the observed and calculated profiles, after fixing the parameters of the upper portion. The top of the PM was determined through four drilled wells which act as control points, while basement surface configurations were estimated by means of iterative fitting. Generally, the model nearly shows the same structural conclusion obtained previously with some modifications on the basement surface. The pre-Evp section was divided into two sections; the Lower-Miocene Rudies Fm. and PM sequence (2440 kg/m^3). The structure shows a noticeable increase in number of faults on the basement surface more than before. The Clysmic faults originate on top of the basement and vanish into the Miocene before reaching the surface. The structure exhibits the same two basinal areas present in south-western part (Khashaba low) and north-eastern portion (W. Bakr basin). The uplifted area between these two basins (W. Bakr area) is characterized by the presence of three local sub-basins separated from each other by saddles, which correspond to West Bakr fields (K, H, G and B).

Basement relief

Source Parameter Imaging (SPI) function was used here as an easy and quick powerful technique for interpreting the gravity data to calculate the approximate depths of gravity sources. The SPI method utilizes the relationship between source depths and the local wavenumber (k) of the observed field, which can be estimated for any point within gridded-data through the horizontal/vertical gradients. The method was carried out to determine depth to causative sources, edge locations, source geometries and density contrast in the area (Nabighian et al 2005). One advantage of the SPI method is that the depths to the sources can be displayed as an image, which makes the task of interpreting the data significantly easier. More elaborate description of the principle, theory, application and formulation of the method are given elsewhere (e.g., Thompson 1982; Roest et al. 1992; Nabighian & Hansen 2001, 2002; Fedi 2005, 2007; Nabighian et al. 2005; Reeves 2005).

Practically, the automatic calculations of source depths were done by using the SPI software included in the Oasis Montage Package 2007. The technique computes source parameters from gridded data of the Bouguer anomaly map based on the complex analytic signal, where depths can be estimated without assumptions about the thickness of the source bodies. The depths to the gravity sources was determined through a number of pre-processed grids dx, dy, and dz which were calculated and serve as inputs for SPI processing. The first order derivative was adhered to remove the deep crustal effect from the original data. The upward continuation for small height was applied because the SPI is very sensitive to noise and interface effect (Nabighian et al. 2005). However, the SPI has the advantages that it produces a more complete set of coherent solution points and is easier to use. The accuracy of SPI is about ±20 % in comparison with the real data from boreholes (Roest et al. 1992).

The results of the depth estimation obtained from application of the SPI method (Fig. 15) exhibits a rough basement surface, with great variation in depth to basement rocks which ranges between 2.25 and 5.75 km. The map delineates three main basinal areas corresponding to the depressions of "Khashaba" to the west, and the "W. Bakr" toward the north-east, and "W. Gharib" to the south-east. These large basins were separated from each other by a broad ridge (West Bakr-Gharib ridge) of relatively low depth. Such basement uplift is considered a focal point in trapping oil from the adjacent basins. Moreover, three narrow sub-basins (Hoshia, Farag and Arta) occupy the northern portion, and are separated from each other by structural highs/saddles. All basins/ridges are nearly trending in the north-west to south-east direction, parallel to the GOS trend. For comparison, Figure 15b displays the approximate depths to gravity sources as deduced from the Bouguer anomaly map (i.e., before stripping). Generally, the map exhibits nearly the same structural conclusion that exists in the former map, but with less details. The disparity between these two figures could be attributed to the gravity effect of the near-surface constituents.

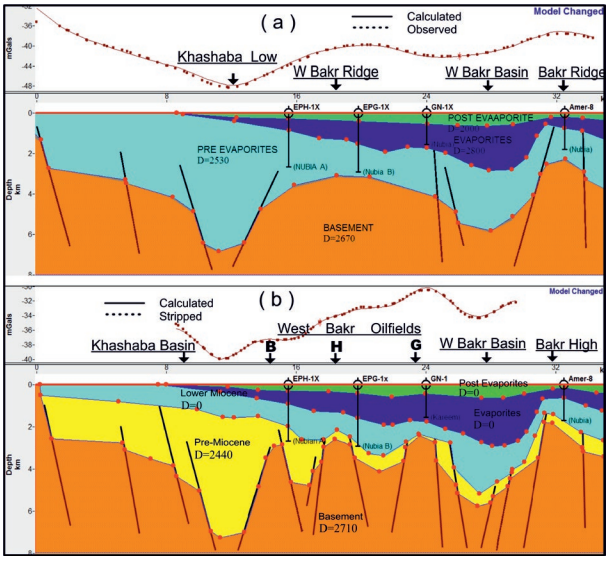

Fig. 14. Gravity modeling along profile B–B' taken (**a**) before doing layer-stripping on Bouguer anomaly map, and (**b**) after doing layer-stripping on top of Pre-Miocene.

Discussion

The seismic lines interpretation has shown a lack of information that comes from the deep subsurface section, while exhibiting a strong reflection from the relatively shallow part. This is logical since the high reflectivity of the Evps makes it difficult to trace any reflections at large depths, where

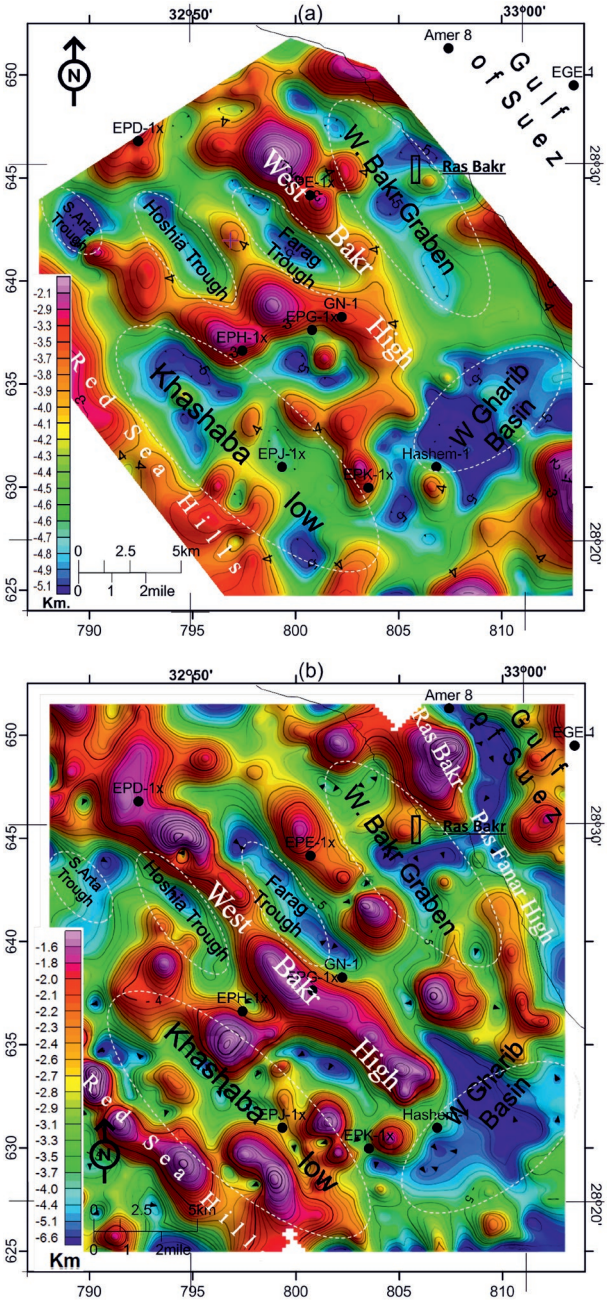

Fig. 15. Basement relief map of the study area as deduced by source parameters imaging (SPI): **a** — after gravity stripping; **b** — before gravity stripping

the continuity of the seismic events became very bad beneath the base of the Evps particularly in the north-eastern side where the thickness of the Evps significantly increases toward the GOS. Thus, the structural maps reveal few or no faults penetrating the base of the Evps, which may be contrary to the reality.

The study demonstrates how gravity interpretation can be enhanced when integrated with seismic data and borehole information in order to reveal the deep structural configurations. The integrated interpretation has overcome the shortcoming of the filtering techniques and also seismic attenuation. The crosschecks between the gravity, seismic and well logging were worked out to eliminate ambiguity as well as non-uniqueness of the gravity data interpretation.

The gravity anomalies are positively affected by the anhydrite of the Ras Malaab Group and/or dense limestone of Gharandal group. Meanwhile, they are negatively influenced by the low density halite/salt rocks, and by the Lower-Miocene Rudeis sands. The non-linear distribution of the density with depth makes most of the filtering methods, especially in space domain, ambiguously interpreted when exploring the deep prospects. So, it is found that the filtering methods applied in this study are rather insufficient in delineating the deep structures/sources at the PM level, especially because seismic interpretation is uncertain. The filtered maps provide primary evidence for deep-seated bodies but add no details. This only minimizes the effect of shallow bodies and somewhat enhances the major features.

The correlation coefficient results are very variable with it reaching the maximum (0.35) against the PM, while attaining the minimum (−0.34) against the Evps. The positive correlation suggests that most of the gravity is sourced in the deep-seated components (PM). However, negative values confirm that effects of these rock units act in reverse to reduce the total gravity.

The horizontal gradient filter was able to disclose the deep fracture systems affecting the area, which were confirmed later by Euler deconvolution solutions that delineated locations of block-faults well. In contrast to the Miocene structure, the PM was ruptured by fractures mainly in the NNW and ENE directions. Such cross-faults are definitely expected to control hydrocarbon migration and accumulation at the PM level, delineating new oilfields.

The statistical analysis of lineaments on top of the PM rocks show that the area was affected by two tectonic trends oriented in the N0–30°W and N50–70°E. These fracture systems are believed to be associated with two stress phases; a compressive phase (NNW–SSE) and an extension phase (ENE–WSW). These two different tectonic forces are closely related to the Tethyan plate tectonics. The first tectonic trend (NNW to NW) is considered one of the oldest tectonic trends in Egypt (Meshref 1990). The structural elements belonging to this tectonic phase are believed to be predominant and most probably developed in Precambrian compression. It was formed during the Pan African orogeny, and rejuvenated during Tertiary–Quaternary times due to active tensional movement of Arabia relative to Africa (Brown & Coleman 1972). It is believed that the ENE folding and thrust-faulting stage was primarily formed in response to the compression force from the NNW–SSE direction. They were developed and reactivated during the Early to mid-Paleozoic (Caledonian cycle) by rift phases resulting from the opening of the Paleo-Tethys under the influence of NE–SW directional tensional forces (Meshref 1990). From the other side, the N50–70°E trend, which is genetically related to the Syrian Arc trend, is believed to be one of the Precambrian/Paleozoic tectonic trends that affect the Egyptian basement and were probably reactivated with the progress of

geological time (El-Emam 1990). The rejuvenation and intensive deformation of this tectonic trend happened during the Late Cretaceous, represented by the NE, ENE & E–W narrow elongated domains of folds and faults (Sehim 1993).

In contrast to the seismic analysis, the modelling after gravity stripping reveals complex structural features at the PM level. The basement surface is uneven and contains swells, troughs and block-faults, of different tilts and throws. The removal of the gravity effects of the upper sedimentary layers, led to the appearance of three gravity highs in the mid-area, which are linked with three PM uplifts. It is reasonable to state that the gravity high anomalies are closely related to basement uplifts, while gravity lows are due to deep sources/structures not shallower than 3 km.

The source parameter imaging method confirms that the actual subsurface situation deduced from the stripped map is not as simple as assumed by the Bouguer anomalies. The map displays uneven topography of the subsurface with presence of several basins and ridges at different depths, which are associated with uplifted and down-faulted basement blocks. The reversals along the sides of the basin-flank highs may give the chance of discovering new oilfields on the PM level.

Conclusion

The results obtained from the different geophysical applications were integrated to give us a general view on the deep source structures and shed more light on geological conditions.

The seismic isopachs indicate that the thickness of the surface layer gradually increases toward the GOS, Miocene Evps increase excessively in the north-east direction, whereas the Lower-Miocene Rudeis sands are well-developed in the south-western part.

The study indicates that the structure on top of the PM is much more complicated than that at the Miocene level. The integrated interpretation has succeeded in delineating several cross-faults on the basement surface which are difficult to see on the seismic sections. This indicates dominance of the NNW-trending faults (Clysmic trend) which were obliquely cut and displaced by ENE-trending faults (Syrian Arc trend).

The structural inferences have depicted that faulting plays the main role in complicating the geological setting of the area. Lineament analysis delimits two fault systems of first order magnitude oriented in the N0–30°W and N50–70°E directions. These two major structural-tectonic trends are the most widespread on the basement surface, and divide the area into segments.

The stress-strain diagram assumes the area has been subjected to two main cycles of tectonism during its geological history; the N5°W compressional force and the N85°E tensional force, producing two pairs of primary and secondary fracture systems. The impact of such tectonic forces on the basement surface may suggest that, although the principal phase of opening of the GOS occurred in the Miocene age, the forces that caused this opening are older.

The models confirm a simple structure at Miocene level in contrast to a complex structure at the PM level. They demonstrate a highly-fractured basement surface, overlain by a heterogeneous sedimentary cover, with no indications of magmatic intrusions penetrating into sediments. They indicate that basement ridges are the source of gravity maxima while the PM basins are the main source of gravity minima.

Acknowledgement: Author would like to express his gratitude to three anonymous reviewers for their constructive reviews and comments, as well as to Miroslav Bielik for editorial handling and suggested improvements to the manuscript.

References

Affleck L. 1963: Magnetic anomaly trend and spacing patterns. *Geophysics* 28, 3, 379–395.

Anderson E.M. 1951: The dynamic of faulting and dyke formation with application to Britain. 2n^{d} Ed. *Oliver and Boyd*, Edinburgh, 1–206.

Azab A.A., Ramadan M.A. & El-Sawy M.Z. 2018: An integrated analysis of gravity and well data for deep-seated structural interpretation: a case study from Ras Budran oilfield Gulf of Suez Egypt. *Journal of Petroleum Exploration and Production Technology*, http: //doi.org/10.1007/s13202–018–0514–8

Bayoumi A. 1983: Tectonic origin of the Gulf of Suez, Egypt, as deduced from gravity data. CRC, *Handbook of Geophysical Explor. At Sea*, 417–432.

Barbosa V., Sliva J. & Medeiros W. 1999: Stability analysis and improvementof structural index in Euler deconvolution. *Geophysics* 64, 48–60

Blakely R.J. 1995: Potential theory in gravity and magnetic applications. *Cambridge Univ. Press*, 1–441.

Bosworth W. & Durocher S. 2017: Present–day stress fields of the Gulf of Suez (Egypt) based on exploratory well data: Non–uniform regional extension and its relation to inherited structures and local plate motion. *Journal of African Earth Sciences* 136, 136–147.

Brown G.F. & Coleman R.G. 1972: The tectonic framework of the Arabian Peninsula. 24th international Geol. Cong. Montreal, Proc. Sect, 3. EGPC, EL Maadi, Cairo, Egypt.

Dimri V.P. 1992: Deconvolution and inverse theory. *Elsevier Science Publishers*, Amsterdam London New York Tokyo.

Fedi M. 2007: DEXP: A fast method to determine the depth and the structural index of potential field sources. *Geophysics* 72, 1–11.

Fedi M., Hansen P.C. & Paoletti V. 2005: Tutorial: Analysis of depth resolution in potential-field inversion. *Geophysics* 70, A1–A11.

El-Emam A. 1990: The Agnes gravity/magnetic anomaly. Implications for potential field geophysics in the Western Desert of Egypt. *10th EGPC Seminar*, Cairo, Egypt, 1–13.

Ghanim M. 1972: Geology of the basement rocks north of Latit. 28^{o} N. Eastern Desert, Ras Gharib Area. *Ann. Geol. Survey*, Cairo, Egypt, II.

GPC 1976: General Petroleum Company, Nasr City, Cairo, Egypt.

Gupta S., Underhill J.R., Sharp I.R. & Gawthorpe R.L. 1999: Role of fault interactions in controlling syn-rift sediment dispersal patterns, Mioc, Abu Alaqa Group, Suez Rift, Sinai, Egypt. *Basin Research* 11, 167–189.

Hammer S. 1963: Deep gravity interpretation by stripping. *Geophysics* Xsviii, 3, 369–378.

Herkat M. & Guiraud R. 2006: The relationships between tectonics and sedimentation in the Late Cretaceous series of the eastern Atlasic Domain Algeria. *Journal of African Earth Sciences* 46, 346–370.

Hinze W.J., von Frese R.R.B. & Saad A.H. 2013: Gravity and magnetic exploration. *Cambridge University Press*, 1–525.

Keating P. & Pilkington M. 2004: Euler deconvolution of the analytic signal and its application to magnetic interpretation. *Geophys. Prospect* 52, 165–182.

Khalil S.M. & McClay K.R. 2008: Structural control on syn-rift sedimentation, northwest Red Sea Margin, Egypt. *Marine and Petroleum Geology* 26, 1018–1034.

Marson L. & Klingele E.E. 1993: Advantage of using the vertical gradient of gravity for 3-D interpretation. *Geophysics* 58, 349–355.

Maus S. & Dimri V.P. 1994: Scaling properties of potential fields due to scaling sources. *Geophys. Res. Lett.* 21, 891–894.

Maus S. & Dimri V.P. 1995: Potential field power spectrum inversion for scaling geology. *J. Geophys. Res.* 100, 12605–12616.

Maus S. & Dimri V.P. 1996: Depth estimation from the scaling power spectrum of potential field. *Geophys. J. Int.* 124, 113–120.

McKinstry H.E. 1953: Shears of the second order. *American Journal of Science* 251, 401–414.

Meshref W. M. & Hammouda H. 1990: Basement tectonic map of northern Egypt. *EGPC, 10th exploration and production Conference*, Cairo, 1–23.

Mostafa A.M. 1976: Block faulting in the Gulf of Suez. *EGPC, 5th Expl. Seminar*, Cairo, 1–19.

Mostafa A.M. 1992: Rifting under sediment loading in the Gulf of Suez, Egypt. *11th Petrol, Explo. Proj. Co.*, Cairo, 1–15.

Nabighian M.N. 1984: Toward a three-dimensional automatic interpretation of potential field data via generalized Hilbert transforms: Fundamental relations. *Geophysics* 49 780–786.

Nabighian M.N. & Hansen R.O. 2001: Unification of Euler and Werner deconvolution in three dimensions via the generalized Hilbert trans form. *Geophysics* 66, 1805–1810.

Nabighian M.N., Grauch V.J.S., Hansen R.O., LaFehr T.R., Li Y., Peirce J.W., Philips J.D. & Ruder M.E. 2005: The historical development of the magnetic method in exploration. *Geophysics* 70, 33–61.

Otsuka T. & Ogawa K. 1977: Combined seismic and gravity interpretation in west Bakr area, Gulf of Suez, Egypt. *Report of Technology Research center, JPC*, Tokyo, 1–6.

Parker R. L. 1973: The rapid calculation of potential anomalies. *Geophysical Journal of the Royal Astronomical Society* 31, 447–455.

Phillips J.D. 1998: Processing and Interpretation of aeromagnetic data for the Santa Cruz Basin-Patahonia Mountains area, South-Central Arizona. *U.S. Geological Survey Open-File Report*, Arizona, 02–98.

Pietrantonio G., Devoti R., Mahmoud S. & Riguzzi F. 2016: Kinematics of the Suez–Sinai area from combined GPS velocity field. *J. Geodyn.* 102, 231–238.

Pilkington M., Gregotski M.E. & Todoeschuck J.P. 1994: Using fractal crustal magnetization models in magnetic interpretation. *Geophysical Prosp.* 42, 677–692.

Reid A.B., Allsop J., Granser H., Millett A.J., Somerton I.W. 1990: Magnetic interpretation in three dimensions using Euler deconvolution. *Geophysics* 55, 80–91.

Reid A., FitzGerald D. & McInerny P. 2003: Euler deconvolution of gravity data. In: 73rd Annual International Meeting Expanded Abstracts. *Society of Exploration Geophysicists*, 580–583.

Reid A.B., Allsop J.M., Granser H., Millett A.J. & Somerton Reeves C.V. 2005: Aeromagnetic Surveys, Principles, Practice and Interpretation. *Geosoft*, 1–155.

Roest W.R., Verhoef J. & Pilkington 1992: Magnetic interpretation using the 3D analytic signal. *Geophysics* 57,116–125.

Rohais S., Barrois A., Colletta B. & Moretti I. 2016: Pre–salt to salt stratigraphic architecture in a rift basin: insights from a basin–scale study of the Gulf of Suez (Egypt). *Arab. J. Geosci.* 9, 317, http: //dx.doi.org/10.1007/s12517–016–2327–8.

Sadek H.S., Rashed S.M. & Blank H.R. 1984: Spectral analysis of aeromagnetic profiles for depth estimation principles, software and practical application. *Open-file report, U. S. Geol. Survey,* Saudi Arab. Project (IR656), 1–40.

Scotte R.W. & Govean F.M. 1984: Early Depositional history of rift basin: Miocene in the Western Sinai. EGPC. *1st Expl. Sem.,* Cairo, 1–15.

Segev A., Avni Y., Shahar J. & Wald R. 2017: Late Oligocene and Miocene different seaways to the Red Sea–Gulf of Suez rift and the Gulf of Aqaba–Dead Sea basins. *Earth Science Reviews* 171, 196–219.

Sehim A. 1993: Cretaceous tectonics in Egypt. *Egypt J. Geol.* 37, 1, 335–372.

Shabaan M.A., El Gindi A. & Abd El Fattah I. 1984: Contribution to the subsurface geology of west Bakr area, Gulf of Suez, Egypt. *Bull. Fac. of Sci.*, Zagazig Univ., 6, 196–217.

Spector A. & Battacharyya K. 1966: Energy density spectrum and subcorrelation function of anomalies due to some simple magnetic models. *Geophysical Prosp.* 14, 242–272.

Spector A. & Grant F.S. 1970: Statistical models for interpreting aeromagnetic data. *Geophysics* 35, 293–302.

Spector A. 1968: Spectral analysis of aeromagnetic maps. *Ph.D. Thesis, Dep. Phys., Faculty of Science, Toronto Univ.*, 1–167.

Thompson D.T. 1982: EULDPH — A new technique for making computer-assisted depth estimates from magnetic data. *Geophysics* 47, 31–37.

Young M.J., Gawthorpe R.L. & Sharp I.R. 2002: Architecture and evolution of syn-rift clastic depositional systems towards the tip of a major fault segment, Suez Rift, Egypt. *Basin Research* 14, 1–23.

Zhang C., Mushayandebvu M.F., Reid A.B., Fairhead J.D. & Odegard M.E. 2000: Euler deconvolution of gravity tensor gradient data. *Geophysics* 65, 512–520.

Appendix

Well	Lat.	Long.
EPK-1x	28°21’43.3” N	32°55’21.9” E
EPJ-1x	28°22’17.9” N	32°52’49.8” E
Hashem-1	28°22’13.2” N	32°57’23.0” E
EPH-1x	28°25’21.4” N	32°51’42.8” E
EPG-1x	28°25’51.6” N	32°53’44.5” E
East Bakr 2	28°28’28.5” N	32°59’29.8” E
EPE-1x	28°29’23.2” N	32°53’44.7” E
EPD-1x	28°25’14.1” N	32°57’04.8” E
EGE 1	28°32’15.1” N	33°01’38.9” E
Amer 8	28°33’12.8” N	32°57’55.7” E
HH 83 1	28°36’36.8” N	32°56’50.1” E
HH 83 2	28°38’33.3” N	32°55’39.9” E